Check for updates

Revealing the crystal facet effect on N₂O formation during the NH₃-SCR over α-MnO₂ catalysts†

Jundong Guo,[a] Fengli Gan,[a] Yifan Zhao,[a] Jinglin He,[a] Bangda Wang,[abc] Tao Gao,[d] Xia Jiang [ID] [abc] and Shenggui Ma [ID] *[abc]

The detailed atomic-level mechanism of the effect induced by engineering the crystal facet of α-MnO₂ catalysts on N₂O formation during ammonia-selective catalytic reduction (NH₃-SCR) was ascertained by combining density functional theory (DFT) calculations and thermodynamics/kinetic analysis. The surface energies of α-MnO₂ with specific (100), (110), and (310) exposed planes were calculated, and the adsorptions of NH₃, NO, and O₂ on three surfaces were analyzed. The adsorption energies showed that NH₃ and NO molecules could be strongly adsorbed on the surface of the α-MnO₂ catalyst, while the adsorption of O₂ was weak. Moreover, the key steps in the oxidative dehydrogenation of NH₃ and the formation of NH₂NO as well as dissociation of NH₂ were studied to evaluate the catalytic ability of NH₃-SCR reaction and N₂ selectivity. The results revealed that the α-MnO₂ catalyst exposed with the (310) plane exhibited the best NH₃-SCR catalytic performance and highest N₂ selectivity, mainly due to its low energy barriers in NH₃ dehydrogenation and NH₂NO generation, and difficulty in NH₂ dissociation. This study deepens the comprehension of the facet-engineering of α-MnO₂ on inhibiting N₂O formation during the NH₃-SCR, and points out a strategy to improve their catalytic ability and N₂ selectivity for the low-temperature NH₃-SCR process.

1 Introduction

Nitrogen oxides (NO_x, including N_2O, NO, and NO_2) emitted from the burning of fossil fuels are one of the main air pollutants in urban areas, and can cause serious environmental problems, such as photochemical smog, acid rain, and ozone depletion.[1–5] In general, 95% of NO_x pollutants are composed of NO, which is toxic and harmful to the health of humans and animals, such as stimulating the lungs and thus triggering many diseases, like cancer and asthma.[6–8] Among various denitrification methods, the selective catalytic reduction process (SCR) using NH_3 as the reducing agent (NH_3-SCR) has been a highly efficient method for removing NO_x emitted from stationary and mobile sources in which NO_x is converted into harmless N_2 and H_2O by the following "Standard SCR" reaction: $4NO + 4NH_3 + O_2 \rightarrow 4N_2 + 6H_2O$.[9,10] However, the non-ignorable byproduct of N_2O generation during the NH_3-SCR process

seems prominently to be: $4NO + 4NH_3 + 3O_2 \rightarrow 4N_2O + 6H_2O$.[11] N_2O has been included in the list of regulated greenhouse gas (GHG) pollutants because of its strong global warming potential, which is 298 times that of CO_2.[12] Therefore, it is a major challenge to restrain the N_2O formation during the high-activity NH_3-SCR process.

A reasonable selection and design of catalysts is an efficient strategy to regulate the NH_3-SCR reaction. Compared with the traditional commercial V_2O_5–WO_3/TiO_2 catalysts, many studies have focused on the development of low-temperature SCR catalysts, including metal oxide-based catalysts, like Fe,[13,14] Mn,[15,16] Ce,[17] Cr,[18] W,[19] Cu,[20,21] and zeolite-based catalysts, like CuSn/ZSM-5 [22] and Cu-ZSM-5.[23] Among various catalysts, manganese-based catalysts have been widely studied and applied due to their low cost and outstanding low-temperature denitrification performance, whereby their abundant Lewis acid sites, variable valence states of Mn, and strong redox ability contribute to their excellent catalytic activity at low temperature, especially under 200 °C.[10,24–27] For instance, Yang *et al.*[28] found that α-MnO₂ exhibited the most superior SCR performance for NO_x conversion compared with other crystal phases of β, γ, and δ-MnO₂ at a lower temperature of 50–120 °C. However, the low N_2 selectivity currently extremely restricts the application of Mn-based catalysts because the strong oxidation ability of tetravalent Mn leads to more N_2O formation.

Manipulating the exposed crystal facets of metal and metal oxide catalysts is an efficient strategy to influence the catalytic

[a]College of Architecture and Environment, Sichuan University, Chengdu 610065, China. E-mail: masgui@scu.edu.cn

[b]College of Carbon Neutrality Future Technology, Sichuan University, Chengdu 610065, China

[c]National Engineering Research Center for Flue Gas Desulfurization, Sichuan University, Chengdu 610065, China

[d]Institute of Atomic and Molecular Physics, Sichuan University, Chengdu 610065, China

† Electronic supplementary information (ESI) available. See DOI: https://doi.org/10.1039/d2ra06744g

activity and selectivity significantly.[29–31] This can be attributed to the different exposed atomic arrangement, distorted electronic structure, and synergistic interactions in the surface of exposed facets. Up to now, three exposed crystal facets, namely the (100), (110), and (310), of the α-MnO$_2$ catalyst were designed to investigate the catalytic activity.[32] α-MnO$_2$ with the exposed high-index facet (310) exhibited a much better activity in the catalytic oxidation of formaldehyde (HCHO) and in the catalytic ozonation of odorous CH$_3$SH thanks to its higher surface energy than α-MnO$_2$ (100) and α-MnO$_2$ (110).[33–35] Whereas, Au/α-MnO$_2$-110 exhibited the highest catalytic activity compared to Au/α-MnO$_2$-100 and Au/α-MnO$_2$-310 in the catalytic combustion of propane because of the lowest oxygen vacancy formation energy of α-MnO$_2$ (110), which benefited the formation of Au$^{\delta+}$ species and therefore promoted the breakage of the C–H bond in propane.[36] Generally, the reactivity and activity of facets are proportional to their surface energy, whereby facets with a high surface energy are usually more reactive in heterogeneous reactions.[37] Unfortunately, the detailed mechanism of the effect induced by engineering the crystal facet of MnO$_2$ on the catalytic ability of the NH$_3$-SCR reaction and N$_2$O formation, as an important issue, have rarely been deeply understood, and thus deserve further investigation.

In view of its adverse effect, many studies have been conducted on the N$_2$O formation mechanism in the NH$_3$-SCR process, in order to contrapuntally put forward effective control solutions. In principle, the favored reaction pathways of the NH$_3$-SCR process were proposed as: (i) NH$_3$ adsorbs on the catalyst surface, getting activated and dissociated to NH$_2$ species, (ii) NO molecules in the gaseous or adsorbed state react with NH$_2$ to form the key NH$_2$NO intermediate species, (iii) NH$_2$NO decomposes into N$_2$ and H$_2$O, (iv) removal of the surface H atoms from the catalyst.[24,38–40] The kinetic estimation revealed that the dehydrogenation of NH$_3$ to NH$_2$ and the formation of NH$_2$NO were rate-limiting steps in the NH$_3$-SCR process, and the reaction of the adsorbed NO with NH$_2$ to generate NH$_2$NO was more kinetically preferred.[24,41] In addition, the strong oxidation ability of Mn-based catalysts can result in the oxidative dehydrogenation of NH$_2$ to NH species, which is inducive to N$_2$O formation.[11] On this account, increasing NH$_2$ species and decreasing NH species are favorable for the NH$_3$-SCR activity and N$_2$ selectivity, which is an effective strategy to screen suitable catalysts. Therefore, the reaction pathways for the dehydrogenation of NH$_3$ and formation of NH$_2$NO could be used to evaluate the catalytic ability and the N$_2$ selectivity during the NH$_3$-SCR reaction with different crystal facets of α-MnO$_2$.

In this article, the crystal facet effect on N$_2$O formation during the NH$_3$-SCR over α-MnO$_2$ catalysts was first evaluated through the DFT+U calculation. The α-MnO$_2$ catalysts with different exposed surfaces, including (100), (110), and (310), were constructed to investigate the effect of engineering the crystal facet at an atomic level. Some key steps of NH$_3$-SCR on MnO$_2$ catalysts have been proposed, including the oxidative dehydrogenation of NH$_3$ to NH$_2$ and then to NH species, which determine the selectivity of the NH$_3$-SCR reaction. The catalytic ability and N$_2$ selectivity were primarily studied by the

thermodynamics and kinetic analysis. This study revealed the crystal facet effect on N$_2$O formation during the NH$_3$-SCR over Mn-based catalysts, and provides a promising strategy for developing robust Mn-based catalysts with good catalytic ability and a high N$_2$ selectivity for the low-temperature NH$_3$-SCR process.

2 Methods

All of the spin-polarized density functional theory (DFT) calculations were implemented in the Vienna ab initio simulation package (VASP).[42,43] The Projector Augmented Wave (PAW) method was used to simulate the interaction between ions and electrons. The Generalized Gradient Approximation (GGA) and Perdew–Burke–Ernzerhof (PBE) exchange–correlation functional were used to deal with the exchange–correlation potential between electrons.[44] In addition, the Mn element in α-MnO$_2$ belonged to the transition metal element of the third period, in which existed a strong Coulomb effect between the electrons in the d layer. Therefore, a DFT+U method was used to correct the strong Coulomb interaction between the 3d electrons in the outer layer of Mn atoms with the values of U_{eff} = 5.5.[45,46] According to reports in the literature, α-MnO$_2$ should be calculated under the antiferromagnetic spin-polarized structure.[47]

For the structural optimization calculations, all the energy of the system converged to 1×10^{-5} eV, and the force on each atom was less than 0.03 eV Å^{-1}. In the static self-consistent field (SCF) calculations, the electronic energies converged to 1×10^{-6} eV. Searches for the transition states along the reaction coordinate were calculated using the climbing image nudged elastic band (CI-NEB) method.[48] All the located transition states were confirmed by vibrational frequency analysis to ensure that there was only one imaginary frequency. The cutoff energy was set to 450 eV and a $4 \times 2 \times 1$ k-point mesh using the Monkhorst–Pack method was used to express the integral of the Brillouin zone. All the electronic energies marked with "E" include the ground state energy of the electron (ε_{ele}) and the contribution of the zero-point vibrational energy (ZPE) calculated by the formula:

$$E = \varepsilon_{ele} + \text{ZPE} \tag{1}$$

where ε_{ele} and ZPE were calculated by VASP and VASPKIT code.[49]

The surface energy (γ) of each surface model was calculated with

$$\gamma = \frac{(E_{slab} - nE_{bulk})}{2A} \tag{2}$$

where E_{slab} is the energy of the surface model, E_{bulk} is the energy of the cell model, n is the number of unit cells that a surface model contains, A represents the area of the slab surface, and 2 represents that each slab model had the same upper and lower surfaces.

To understand the strength of the adsorption between the gas molecules and the catalyst surface, the adsorption energy (E_{ads}) was calculated according to the following formula:

$$E_{\text{ads}} = E_{(\text{adsorbate/surface})} - E_{(\text{surface})} - E_{(\text{adsorbate})} \quad (3)$$

where $E_{(\text{adsorbate/surface})}$, $E_{(\text{surface})}$, and $E_{(\text{adsorbate})}$ represent the total energy of the adsorbate adsorbed to the catalyst surface, the energy of the surface model, and the energy of the adsorbate (gas molecules), respectively.

The reaction energy (ΔE_{rxn}) and energy barrier (E_{a}) of each elementary reaction were calculated using the following formulas:

$$\Delta E_{\text{rxn}} = E_{\text{FS}} - E_{\text{IS}} \quad (4)$$

$$E_{\text{a}} = E_{\text{TS}} - E_{\text{IS}} \quad (5)$$

where E_{IS}, E_{TS}, and E_{FS} represent the total energy of the reaction initial state, transition state, and final state, respectively.

To understand the effect of temperature on the reaction, the calculated energies (E) were corrected for the Gibbs free energy (G) in the following formulas:[27]

$$G_{\text{gas}} = \varepsilon_{\text{ele}} + \text{ZPE} + \Delta G_{0 \to T} \quad (6)$$

$$G_{\text{solid}} = \varepsilon_{\text{ele}} + \text{ZPE} + \Delta U_{0 \to T} - TS \quad (7)$$

where ε_{ele} is the electron energy of the system in the ground state, ZPE is the zero-point correction energy, T is the temperature, S is the entropy of the system, and $\Delta U_{0 \to T}$ and $\Delta G_{0 \to T}$ are the contribution of the temperature to enthalpy and the Gibbs free energy. Also, G_{gas} represents the energy of gas molecules and G_{solid} represents the energy of catalysts and adsorbed species. All the thermodynamic quantities were processed with VASPKIT code.[49]

In order to better measure the speed of each elementary reaction, the reaction rate constant k was calculated according to the transition state theory (TST)[50] as per the following formula:

$$k = \frac{K_{\text{B}}T}{h} e^{-\frac{G_{\text{a}}}{K_{\text{B}}T}} \quad (8)$$

where K_{B} is the Boltzmann constant (1.380649×10^{-23} J K^{-1}), h is Planck's constant ($6.62607015 \times 10^{-34}$ J s), T is the temperature (K), and G_{a} is the energy barrier with the correction for the Gibbs free energy from E_{a} through formulas (5)–(7).

3 Results and discussion

3.1 Models and surface energies

The cell model structure of α-MnO$_2$ was established first (Fig. 1a), in which it has a (2×2) tunnel structure and the space group $I4/m$.[47,51] with the relaxation lattice constants obtained by geometric optimization as $a = b = 9.850$ Å, $c = 2.925$ Å. As shown in Fig. 1b–d, the surface models of α-MnO$_2$ with three crystal facets of (100), (110), and (310) were constructed to further understand the difference in the exposed facets of α-MnO$_2$ and its effect on N$_2$O formation. All the models maintained stoichiometric MnO$_2$ ratios and proper surface sites for the adsorption of gas molecules. A vacuum layer of 15 Å was added to the three models to avoid the interaction between the
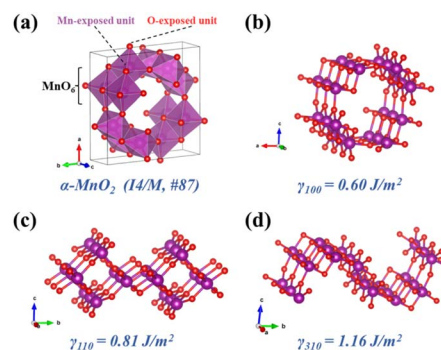

Fig. 1 Crystal structure of (a) bulk α-MnO$_2$, (b) α-MnO$_2$ (100), (c) α-MnO$_2$ (110), and (d) α-MnO$_2$ (310). Purple and red circles denote Mn and O atoms, respectively.

slabs in the z-direction. The calculated surface energies of the slab models of α-MnO$_2$ (100), (110), and (310) were 0.60, 0.81, and 1.16 J m^{-2} respectively, which indicated that α-MnO$_2$ (100) had thermodynamically stable facets with the lowest surface energy.

3.2 Adsorption of gas molecules

The adsorption and activation of reactant molecules on the active sites of catalysts are regarded as important steps in the NH$_3$-SCR process. Three key gas molecules (NH$_3$, NO, and O$_2$)[52] in the NH$_3$-SCR process on α-MnO$_2$ catalysts with three crystal facets were tested first to obtain their adsorption energy and the most favorable adsorption site. The test results are shown in Fig. S1† and the optimum configurations are shown in Fig. 2. It can be concluded the NH$_3$ molecules were easily adsorbed on the α-MnO$_2$ surface, with the N atom bonding to the surface Mn atom, where the Mn cations acted as a Lewis acid site to have more empty orbitals to accept electron pairs.[53,54] The calculated adsorption energies of NH$_3$ molecules on the surfaces of α-MnO$_2$ (100), (110), and (310) were −1.12, −1.82, and −1.08 eV, respectively, as shown in Table 1, which all had strong chemical

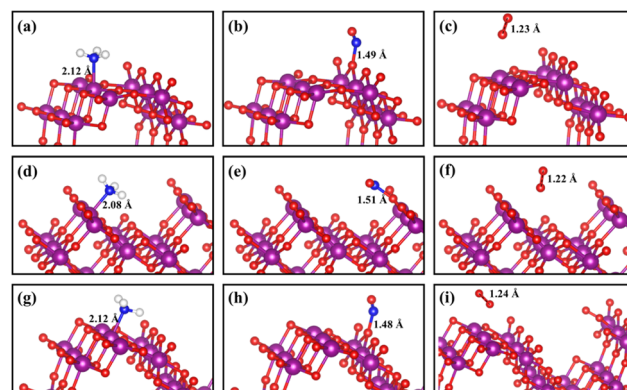**Fig. 2** Adsorption configurations of NH$_3$, NO, and O$_2$ molecules on α-MnO$_2$ surfaces with different crystal facets: (a–c) (100); (d–f) (110); (g–i) (310). Purple, red, dark blue, and white circles denote Mn, O, N, and H atoms, respectively.

Table 1 Adsorption energies (eV) of three gas molecules on α-MnO$_2$ (100), (110), and (310) facets with zero-point vibrational energy (ZPE) contribution

	NH$_3$	NO	O$_2$
(100)	−1.12	−2.23	−0.05
(110)	−1.82	−2.64	−0.27
(310)	−1.08	−1.96	−0.09

adsorption with the catalysts and showed a table-shaped exothermic process.

The charge-density difference of NH$_3$ molecule adsorbed on α-MnO$_2$ surfaces, as shown in Fig. 3a, demonstrated that there was more electron consumption around the H atom and more electron accumulation around the N atom, which showed that part of the electrons were transferred from the H atom to N atom. In the adsorption site, especially around the Mn atom, there was more electron accumulation, which illustrated that electrons were transferred from NH$_3$ to α-MnO$_2$ catalysts. The NH$_3$ molecules acted as electron donors in the adsorption on α-MnO$_2$ (100), (110), and (310) surfaces, which lost 0.25e, 0.28e, and 0.21e, respectively, by Bader charge analysis, as shown in Fig. 3b. The calculated results verified the role of the Lewis acid site that the Mn atom behaved as, which may facilitate the activation of NH$_3$ in the NH$_3$-SCR process.[55]

The adsorption of NO molecules on α-MnO$_2$ (100) (110), and (310) facets are also shown in Fig. 2. Different from the results of the NH$_3$ molecules, NO molecules preferred the O site, forming an O–N–O structure, which indicated that no competitive adsorption occurred between NH$_3$ and NO molecules over α-MnO$_2$. The calculated adsorption energies on three facets were −2.23, −2.64, and −1.96 eV, as listed in Table 1, which all presented a strong process of chemical adsorption. The Bader charges analysis displayed that NO molecules acted as electron acceptors after adsorption, which obtained 0.77e, 0.74e, and 0.75e on α-MnO$_2$ (100) (110), and (310), respectively.

For O$_2$ molecules, the optimized adsorption configurations showed that they did not tend to be bonded on the surface. The adsorption energies of O$_2$ on the (100), (110), and (310) surfaces were −0.05, −0.27, and −0.09 eV, respectively. All of them were

less than 0.5 eV, coinciding with the results from the adsorption of O$_2$ on the surface of β-MnO$_2$.[56] Only weak physical adsorption of O$_2$ molecule could happen on pure α-MnO$_2$ surfaces, which indicated that O$_2$ could not directly be chemisorbed on the catalysts surface. Instead, physically adsorbed O$_2$ molecule could react with the surface-active species, such as intermediate H atom to form *OH and H$_2$O, to participate in the reaction in the NH$_3$-SCR process.[24,56] Besides, O$_2$ could also be activated by the defected slab containing an oxygen vacancy.[24] It is reported that α-MnO$_2$ (310) has the lowest formation energy of an oxygen vacancy of 0.33 eV than that of (100) and (110),[33] which indicates that the O$_2$ molecule is beneficial to be adsorbed and dissociated on defected the α-MnO$_2$ (310) surface to participate in the removal of surface H atom and the generation of H$_2$O.

3.3 Key reaction pathways

The schemed reaction pathways depicted in Fig. 4 have been widely employed to illuminate the mechanism of N$_2$O formation during the NH$_3$-SCR reaction. Here, the three key reaction steps of the dehydrogenation of NH$_3$ and formation of NH$_2$NO were used to evaluate the NH$_3$-SCR catalytic ability and the N$_2$ selectivity discussed in the introduction of this paper: step R1: NH$_3$ → NH$_2$ + H, where the activated NH$_3$ dissociated to NH$_2$ species; step R2: NH$_2$ + NO → NH$_2$NO, where the NO reacts with NH$_2$ to form the NH$_2$NO following the L–H mechanism; step R3: NH$_2$ → NH + H, where the NH$_2$ species are oxidized to NH. The energy profiles of R1, R2, and R3 over the three surfaces of α-MnO$_2$ (100) (110), and (310) and the corresponding geometries of all the intermediates and transition states are depicted in Fig. 5–7. The values of the energy barriers and reaction energies for the R1–3 reactions over the three crystal facets of α-MnO$_2$ are summarized in Table 2.

Starting from the reaction for R1, an NH$_3$ molecule was adsorbed and activated by the catalysts while the adjacent O site on the catalyst surface acted as a fitted acceptor for H atoms in the NH$_3$ molecule, enlarging the distance between H and NH$_2$. At the end of this reaction, a H atom dissociated from the NH$_3$ molecule combined with surface oxygen atoms to form
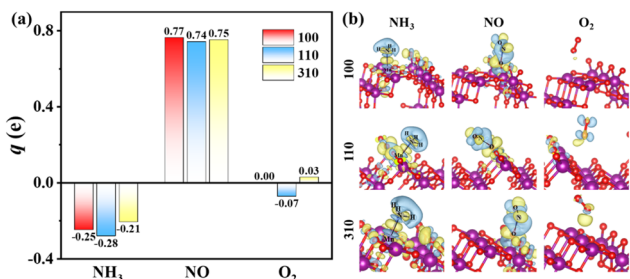

Fig. 3 (a) Bader charges variations of NH$_3$, NO, and O$_2$ molecules adsorbed on α-MnO$_2$ (100), (110), and (310) facets. (b) Charge-density differences of the adsorption structures. Blue and yellow density regions represent electron density depletion and accumulation respectively (isosurface levels set as 0.0025 e Å^{-3}).
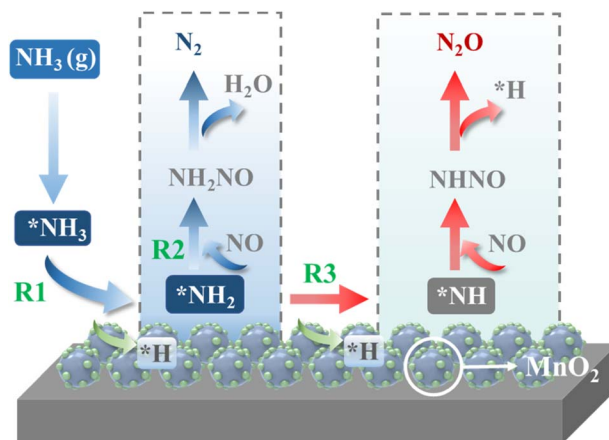

Fig. 4 Schematic of the reaction pathways for N$_2$ and N$_2$O formation during the NH$_3$-SCR reaction over MnO$_2$.
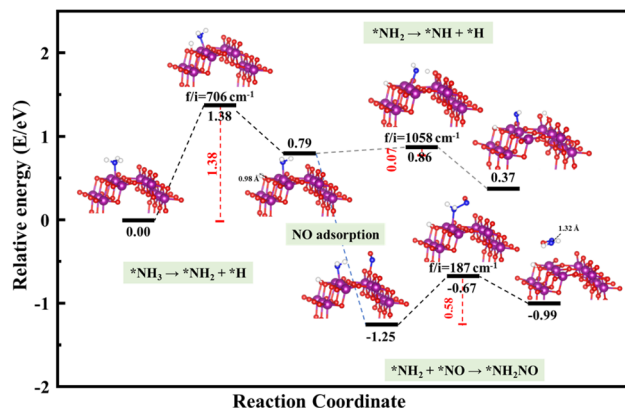
Fig. 5 Reaction pathway for R1–3 over α-MnO$_2$ (100) coupled with the calculated structures. Purple, red, dark blue, and white circles denote Mn, O, N, and H atoms, respectively.
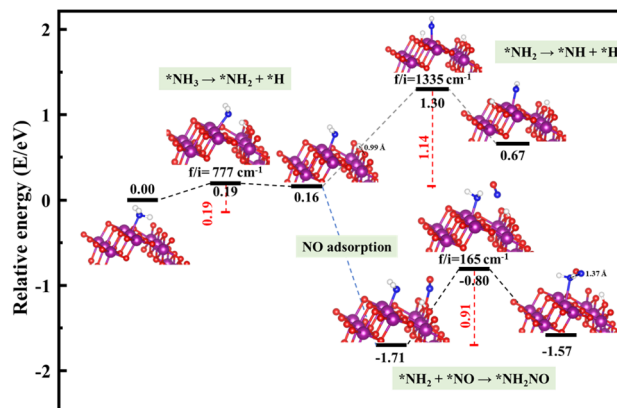

Fig. 6 Reaction pathway for R1–3 over α-MnO$_2$ (110) coupled with the calculated structures. Purple, red, dark blue, and white circles denote Mn, O, N, and H atoms, respectively.

Fig. 7 Reaction pathway for R1–3 over α-MnO$_2$ (310) coupled with the calculated structures. Purple, red, dark blue, and white circles denote Mn, O, N, and H atoms, respectively.
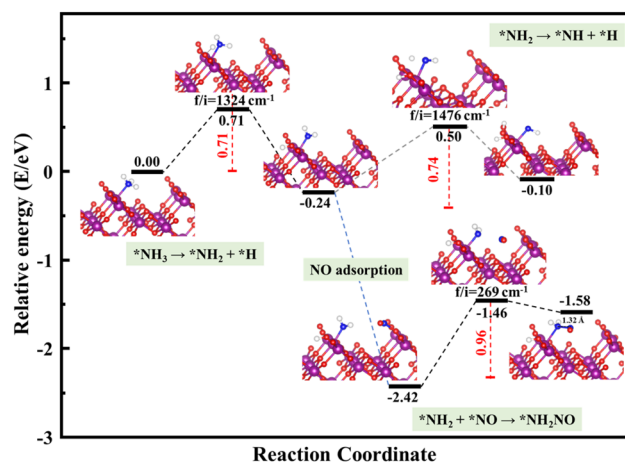
Table 2 Energy barriers (E_a, eV) and reaction energies (ΔE_{rxn}, eV) of three elementary reactions on α-MnO$_2$ (100), (110), and (310) facets

		(100)		(110)		(310)	
Step	Elementary reaction	E_a	ΔE_{rxn}	E_a	ΔE_{rxn}	E_a	ΔE_{rxn}
R1	NH$_3$ → NH$_2$ + H	1.38	0.79	0.71	−0.24	0.19	0.16
R2	NH$_2$ + NO → NH$_2$NO	0.58	0.26	0.96	0.84	0.91	0.14
R3	NH$_2$ → NH + H	0.07	−0.42	0.74	0.14	1.14	0.51

N$_2$O, the further oxidative dehydrogenation of NH$_2$ to NH (the process for R3) was also investigated. After one H atom dissociated from the NH$_3$ molecule to the surface O atom on the α-MnO$_2$ surface, another H atom dissociated from NH$_2$ species to the adjacent oxygen site of the catalyst surface. Our results showed that all the processes on the three catalysts were endothermic with positive reaction energy. The reaction energies of this reaction on α-MnO$_2$ (100), (110), and (310) were 0.07, 0.74, and 0.91 eV, respectively. It is worth noting that the NH$_2$ intermediate could be easily converted into NH species over the α-MnO$_2$ (100) with a low energy barrier of 0.07 eV, resulting in poor reactivity and N$_2$ selectivity.

Overall, α-MnO$_2$ (100) had high NH$_3$ dissociation (1.38 eV) and low NH$_2$ dissociation (0.07 eV) energy barriers, which means it faces the problem of poor activity and nitrogen selectivity. The energy barriers of NH$_3$ dissociation and NH$_2$NO generation on α-MnO$_2$ (110) were 0.71 and 0.96 eV, which were similar to the reported results of 1.10 eV on α-MnO$_2$ (110) and lower than the results of 1.15 eV on γ-Fe$_2$O$_3$ (110) and 1.27 eV on CeO$_2$ (111).[38] However, the high-index facet of α-MnO$_2$ (310) had a low energy barrier for NH$_3$ dissociation (0.19 eV) and a high energy barrier for NH formation (1.14 eV), which exhibited the excellent reaction activity and good N$_2$ selectivity compared with the (100) and (110) facets.

3.4 Thermodynamic and kinetic analysis

Temperature plays an important role in the NH$_3$-SCR process. Therefore, the variations of the reaction energy of each

a hydroxyl group, and the final O–H bond lengths on the three crystal facets were 0.98, 0.98, and 0.99 Å, respectively. The calculated results showed that the process of NH$_3$ dissociation on the α-MnO$_2$ (100) and (310) surfaces was endothermic for both, with reaction energies of 0.79 and 0.16 eV. However, it was slightly exergic for NH$_3$ dissociating on the surface of α-MnO$_2$ (110), with a reaction energy of −0.24 eV. Moreover, α-MnO$_2$ (100) had the highest energy barrier (1.38 eV) for NH$_3$ dissociation compared to α-MnO$_2$ (110) and (310), indicating that the difficulty in dissociation of NH$_3$ may be the key factor to reduce its SCR activity. The (310) facet had the lowest energy barrier of 0.19 eV for NH$_3$ to dissociate, which would be more favorable to activate the NH$_3$ molecule and facilitate the SCR process.

Subsequently, the NO molecule desorbed from the O site approached the NH$_2$ species and bonded to the N atom to form the NH$_2$NO intermediate (the process for R2), with N–N bond lengths of 1.32, 1.32, and 1.37 Å on the (100), (110), and (310) facets, respectively. The calculated energy barriers were 0.58, 0.96, and 0.91 eV, respectively. Concerning the formation of
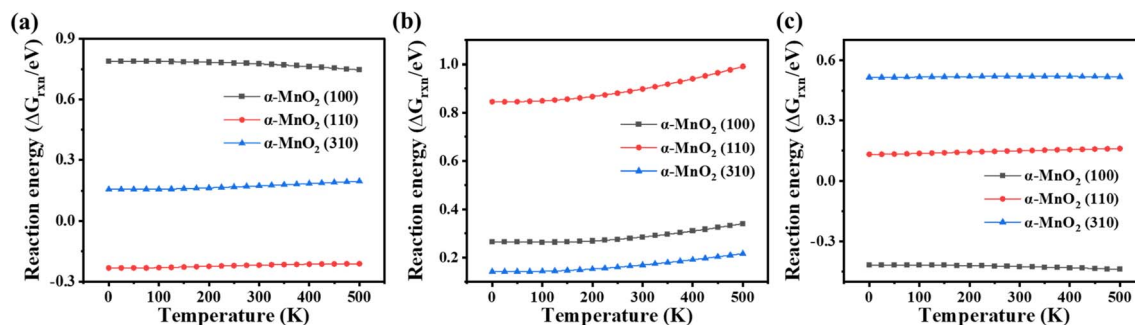
Fig. 8 Variation of the reaction free energy value (ΔG_{rxn}) under different temperatures for R1–3. (a) NH$_3$ dissociation, (b) NH$_2$NO generation, and (c) NH$_2$ dissociation.

elementary reaction were analyzed by the correction of the Gibbs free energy (formulas (4)–(7)) to obtain the thermodynamic properties. The reaction energies with the correction for the Gibbs free energy of processes R1–3 on α-MnO$_2$ exposing different crystal facets at temperatures below 500 K were plotted, and are shown in Fig. 8. The results indicated that for α-MnO$_2$ (100), the high ΔG_{rxn} of R1 restricted the dissociation of NH$_3$. Besides, as the temperature decreased, the reaction free energy value of R1 on α-MnO$_2$ (100) became more positive, which became more limited. The reaction for NH$_2$ dissociation was exergonic on α-MnO$_2$ (100), and spontaneous as well, which could lead to poor N$_2$ selectivity. For α-MnO$_2$ (110), the reaction of NH$_3$ dissociation was exergonic, and had a certain spontaneity. As the temperature decreased, the ΔG_{rxn} of NH$_2$NO generation on α-MnO$_2$ (110) became less exergonic, but its higher reaction free energy value than that of α-MnO$_2$ (100) and (310) still restricted this reaction and led to a poor catalytic activity. The reaction free energy values of R1 and R2 on α-MnO$_2$ (310) both decreased with the decrease in temperature, keeping at a low endergonic value. Moreover, the ΔG_{rxn} value of R3 on α-MnO$_2$ (310) was higher than that of R1 and R2, as well as on α-

MnO$_2$ (100) and (110), showing it was the thermodynamically rate-limiting step, indicating that α-MnO$_2$ (310) had good catalytic activity and N$_2$ selectivity.

According to the reaction pathway for R1–3, the rate-determining steps could be obtained by formula (8) to perform the kinetic analysis. The reaction rate constants (k) for R1–3 below 500 K are listed in Table S1† and the natural logarithm data ln(k) are plotted in Fig. 9, respectively. The results showed that the rate of reactions R1–3 decreased with the reaction temperature decreasing, especially for the dehydrogenation of NH$_3$ on α-MnO$_2$ (100) and dissociation of NH$_2$ on α-MnO$_2$ (310). Moreover, the (100) had a slightly higher rate constant for the N$_2$O generation than those of the other facets. In particular, the reaction rate constants of R1 and R2 were much larger than that of R3 on α-MnO$_2$ (310) at the research temperatures, indicating that the (310) facet showed remarkable activity and N$_2$ selectivity, in line with the results from the reaction pathway analysis.

4   Conclusions

In summary, the effect induced by engineering the crystal facet of α-MnO$_2$ catalysts on N$_2$O formation during the NH$_3$-SCR were systematically investigated by using DFT+U calculations. The adsorption behavior of the key gas molecules in the NH$_3$-SCR process was described by configurations of the gas adsorption on three surfaces of α-MnO$_2$ (100), (110), and (310). It could be found that the NH$_3$ molecule prefers the Lewis acid site (the Mn site) on the α-MnO$_2$ surface, but the NO molecule tends to adsorb on the O site, with both showing strong chemical adsorption. The adsorption energy of the NH$_3$ and NO molecules on the α-MnO$_2$ (110) surface was higher than that of O$_2$. Three key reaction pathways for the dehydrogenation of NH$_3$, formation of NH$_2$NO, and dissociation of NH$_2$ were considered to construct the reaction activity and N$_2$ selectivity. The detailed path for N$_2$O formation was explored by the transition state theory. The effects of different reaction temperatures on the reaction equilibrium and reaction rate were revealed in depth through thermodynamics and kinetics analyses. The results suggested that the high-index facet of α-MnO$_2$ (310) exhibited excellent reaction activity and good N$_2$ selectivity compared with the (100) and (110) facets in the researched temperature range
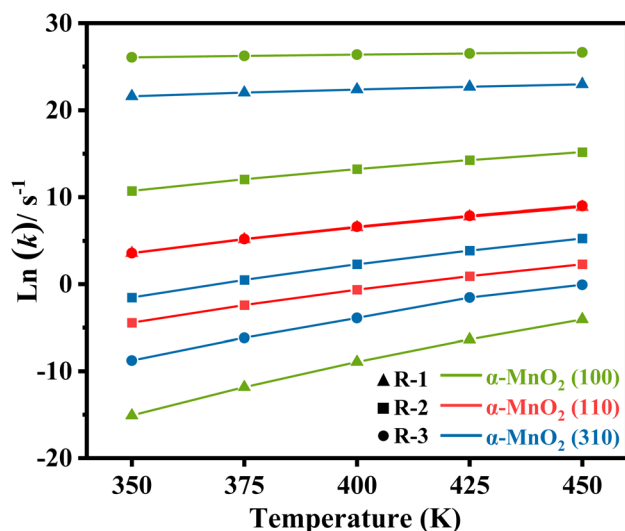

Fig. 9 Natural logarithm of the reaction rate constant (k) of R1–3 under different temperatures.

below 500 K. The findings of this study help improve the atomic-level knowledge of the mechanism of N_2O formation, and advance the understanding of the roles of the crystal facets of α-MnO_2 on the denitration activity and selectivity, which is good reference for the suppression of N_2O emission during the low-temperature NH_3-SCR.

Author contributions

Jundong Guo: conceptualization, methodology, formal analysis, resources, data curation, writing – original draft, visualization; Fengli Gan: resources, investigation, visualization; Yifan Zhao: resources, investigation, data curation; Jinglin He: resources, investigation, visualization; Tao Gao: formal analysis, software; Xia Jiang: writing – review & editing, supervision, project administration, funding acquisition; Shenggui Ma: methodology, formal analysis, writing – review & editing, supervision, funding acquisition.

Conflicts of interest

There are no conflicts of interest to declare.

Acknowledgements

Notes and references

1 G. Jiang, X. Li, M. Lan, T. Shen, X. Lv, F. Dong and S. Zhang, *Appl. Catal., B*, 2017, **205**, 532–540.

2 Q. Zhang, Y. Huang, L. Xu, J.-j. Cao, W. Ho and S. C. Lee, *ACS Appl. Mater. Interfaces*, 2016, **8**, 4165–4174.

3 H. Schneider, S. Tschudin, M. Schneider, A. Wokaun and A. Baiker, *J. Catal.*, 1994, **147**, 5–14.

4 R. Tsekov and P. G. Smirniotis, *J. Phys. Chem. B*, 1998, **102**, 9525–9531.

5 H.-F. Wang, Y.-L. Guo, G. Lu and P. Hu, *J. Phys. Chem. C*, 2009, **113**, 18746–18752.

6 L. Zhao, G. Dong, L. Zhang, Y. Lu and Y. Huang, *ACS Appl. Mater. Interfaces*, 2019, **11**, 10042–10051.

7 D. P. Chock, A. M. Dunker, S. Kumar and C. S. Sloane, *Environ. Sci. Technol.*, 1981, **15**, 933–939.

8 I. M. Orme, R. T. Robinson and A. M. Cooper, *Nat. Immunol.*, 2015, **16**, 57–63.

9 J.-K. Lai and I. E. Wachs, *ACS Catal.*, 2018, **8**, 6537–6551.

10 L. Han, S. Cai, M. Gao, J.-y. Hasegawa, P. Wang, J. Zhang, L. Shi and D. Zhang, *Chem. Rev.*, 2019, **119**, 10916–10976.

11 S. Yang, S. Xiong, Y. Liao, X. Xiao, F. Qi, Y. Peng, Y. Fu, W. Shan and J. Li, *Environ. Sci. Technol.*, 2014, **48**, 10354–10362.

12 A. Ravishankara, J. S. Daniel and R. W. Portmann, *Science*, 2009, **326**, 123–125.

13 M. Gao, G. He, W. Zhang, J. Du and H. He, *Environ. Sci. Technol.*, 2021, **55**, 10967–10974.

14 W. Yang, J. Ren, H. Zhang, J. Li, C. Wu, I. D. Gates and Z. Gao, *Fuel*, 2021, **302**, 121041.

15 Z. Fu, G. Zhang, W. Han and Z. Tang, *Chem. Eng. J.*, 2021, **426**, 131334.

16 Y. Xin, H. Li, N. Zhang, Q. Li, Z. Zhang, X. Cao, P. Hu, L. Zheng and J. A. Anderson, *ACS Catal.*, 2018, **8**, 4937–4949.

17 X. Sun, R.-t. Guo, S.-w. Liu, J. Liu, W.-g. Pan, X. Shi, H. Qin, Z.-y. Wang, Z.-z. Qiu and X.-y. Liu, *Appl. Surf. Sci.*, 2018, **462**, 187–193.

18 P. G. Smirniotis, D. A. Peña and B. S. Uphade, *Angew. Chem., Int. Ed.*, 2001, **40**, 2479–2482.

19 Y. Inomata, H. Kubota, S. Hata, E. Kiyonaga, K. Morita, K. Yoshida, N. Sakaguchi, T. Toyao, K.-i. Shimizu and S. Ishikawa, *Nat. Commun.*, 2021, **12**, 1–11.

20 C. Chen, Y. Cao, S. Liu and W. Jia, *Appl. Surf. Sci.*, 2020, **507**, 145153.

21 S. Hao, Y. L. Liu and J. Yang, *Sci. Total Environ.*, 2022, **820**, 152984.

22 K. Lee, B. Choi, C. Kim, C. Lee and K. Oh, *J. Ind. Eng. Chem.*, 2021, **93**, 461–475.

23 J. Cheng, R. Xu, N. Liu, C. Dai, G. Yu, N. Wang and B. Chen, *Catal. Sci. Technol.*, 2022, **12**, 823–833.

24 H. Yuan, N. Sun, J. Chen, J. Jin, H. Wang and P. Hu, *ACS Catal.*, 2018, **8**, 9269–9279.

25 X. Shi, J. Guo, T. Shen, A. Fan, Y. Liu and S. Yuan, *J. Taiwan Inst. Chem. Eng.*, 2021, **126**, 102–111.

26 L.-g. Wei, R.-t. Guo, J. Zhou, B. Qin, X. Chen, Z.-x. Bi and W.-g. Pan, *Fuel*, 2022, **316**, 123438.

27 B. Tian, S. Ma, J. Guo, Y. Zhao, T. Gao and X. Jiang, *Appl. Surf. Sci.*, 2022, **601**, 154162.

28 J. Yang, S. Ren, B. Su, G. Hu, L. Jiang, J. Cao, W. Liu, L. Yao, M. Kong and J. Yang, *Catal. Lett.*, 2021, **151**, 2964–2971.

29 R. Yang, S. Peng, B. Lan, M. Sun, Z. Zhou, C. Sun, Z. Gao, G. Xing and L. Yu, *Small*, 2021, **17**, 2102408.

30 B. Hu, K. Sun, Z. Zhuang, Z. Chen, S. Liu, W. C. Cheong, C. Chen, M. Hu, X. Cao and J. Ma, *Adv. Mater.*, 2022, 2107721.

31 B. Jiang, Y. Qiu, D. Tian, Y. Zhang, X. Song, C. Zhao, M. Wang, X. Sun, H. Huang and C. Zhao, *Adv. Energy Mater.*, 2021, 2102995.

32 R. Yang, Y. Fan, R. Ye, Y. Tang, X. Cao, Z. Yin and Z. Zeng, *Adv. Mater.*, 2021, **33**, 2004862.

33 S. Rong, P. Zhang, F. Liu and Y. Yang, *ACS Catal.*, 2018, **8**, 3435–3446.

34 D. Ding, Y. Zhou, T. He and S. Rong, *Chem. Eng. J.*, 2022, **431**, 133737.

35 C. He, Y. Wang, Z. Li, Y. Huang, Y. Liao, D. Xia and S. Lee, *Environ. Sci. Technol.*, 2020, **54**, 12771–12783.

36 Y. Jian, Z. Jiang, C. He, M. Tian, W. Song, G. Gao and S. Chai, *Catal. Sci. Technol.*, 2021, **11**, 1089–1097.

37 Q. Kuang, X. Wang, Z. Jiang, Z. Xie and L. Zheng, *Acc. Chem. Res.*, 2014, **47**, 308–318.

38 G. He, M. Gao, Y. Peng, Y. Yu, W. Shan and H. He, *Environ. Sci. Technol.*, 2021, **55**, 6995–7003.

39 S. Yang, Y. Liao, S. Xiong, F. Qi, H. Dang, X. Xiao and J. Li, *J. Phys. Chem. C*, 2014, **118**, 21500–21508.

40 Z. Chen, F. Wang, H. Li, Q. Yang, L. Wang and X. Li, *Ind. Eng. Chem. Res.*, 2012, **51**, 202–212.

41 M. Zhang, W. Wang and Y. Chen, *Phys. Chem. Chem. Phys.*, 2018, **20**, 2211–2219.

42 G. Kresse and J. Hafner, *Phys. Rev. B: Condens. Matter Mater. Phys.*, 1993, **48**, 13115.

43 G. Kresse and J. Furthmüller, *Phys. Rev. B: Condens. Matter Mater. Phys.*, 1996, **54**, 11169.

44 J. P. Perdew, K. Burke and M. Ernzerhof, *Phys. Rev. Lett.*, 1996, **77**, 3865.

45 D. A. Tompsett, D. S. Middlemiss and M. S. Islam, *Phys. Rev. B: Condens. Matter Mater. Phys.*, 2012, **86**, 205126.

46 X. Ye, X. Jiang, L. Chen, W. Jiang, H. Wang, W. Cen and S. Ma, *Appl. Surf. Sci.*, 2020, **521**, 146477.

47 E. Cockayne and L. Li, *Chem. Phys. Lett.*, 2012, **544**, 53–58.

48 G. Henkelman and H. Jónsson, *J. Chem. Phys.*, 2000, **113**, 9978–9985.

49 V. Wang, N. Xu, J.-C. Liu, G. Tang and W.-T. Geng, *Comput. Phys. Commun.*, 2021, **267**, 108033.

50 S. Canneaux, F. Bohr and E. Henon, *J. Comput. Chem.*, 2014, **35**, 82–93.

51 L. Espinal, W. Wong-Ng, J. A. Kaduk, A. J. Allen, C. R. Snyder, C. Chiu, D. W. Siderius, L. Li, E. Cockayne and A. E. Espinal, *J. Am. Chem. Soc.*, 2012, **134**, 7944–7951.

52 D. Wang, Q. Chen, X. Zhang, C. Gao, B. Wang, X. Huang, Y. Peng, J. Li, C. Lu and J. Crittenden, *Environ. Sci. Technol.*, 2021, **55**, 2743–2766.

53 Y. Peng, W. Yu, W. Su, X. Huang and J. Li, *Catal. Today*, 2015, **242**, 300–307.

54 Y. Wang, L. Chen, H. Cao, Z. Chi, C. Chen, X. Duan, Y. Xie, F. Qi, W. Song and J. Liu, *Appl. Catal., B*, 2019, **245**, 546–554.

55 F. Lin, Q. Wang, J. Zhang, J. Jin, S. Lu and J. Yan, *Ind. Eng. Chem. Res.*, 2019, **58**, 22763–22770.

56 X. J. Zhou, Y. Sun, B. Zhu, J. Chen, J. Xu, H. Yu and M. Xu, *Fuel*, 2022, **318**, 123470.